Forward baryons in relativistic nucleus-nucleus collisions

J. Barrette,[1] R. Bellwied,[2] P. Braun-Munzinger,[2] W. E. Cleland,[3] G. David,[2] J. Dee,[2] M. Fatyga,[4] D. Fox,[5] S. V. Greene,[6] J. Hall,[7] T. K. Hemmick,[2] R. Heifetz,[8] N. Herrmann,[9] R. W. Hogue,[4] G. Ingold,[2] K. Jayananda,[3] D. Kraus,[3] B. Shiva Kumar,[6] M. Lisa,[2] D. Lissauer,[4] W. J. Llope,[2] T. Ludlam,[4] R. Majka,[6] D. Makowiecki,[4] S. K. Mark,[1] J. T. Mitchell,[6] M. Muthuswamy,[2] E. O'Brien,[4] V. Polychronakos,[4] C. Pruneau,[1] F. Rotondo,[6] J. Sandweiss,[6] J. Simon,[10] U. Sonnadara,[3] J. Stachel,[2] H. Takai,[4] T. Throwe[4] L. Waters,[2] C. Winter,[6] C. Woody,[4] K. Wolf,[10] D. Wolfe,[7] and Y. Zhang[2]

(E814 Collaboration)

[1]*McGill University, Montreal, Canada H3A 2T8*
[2]*State University of New York, Stony Brook, New York 11794*
[3]*University of Pittsburgh, Pittsburgh, Pennsylvania 15260*
[4]*Brookhaven National Laboratory, Upton, New York 11973*
[5]*Los Alamos National Laboratory, Los Alamos, New Mexico 87545*
[6]*Yale University, New Haven, Connecticut 06511*
[7]*University of New Mexico, Albuquerque, New Mexico 87131*
[8]*University of Tel Aviv, Tel Aviv, Israel*
[9]*Gesellschaft fuer Schwerionenforschung, 61 Darmstadt, Germany*
[10]*Texas A&M University, College Station, Texas 77843*

(Received 23 July 1991)

We present the rapidity and transverse momentum distributions of protons and neutrons from collisions between 14.6 GeV/nucleon beams of ^{28}Si and targets of Al, Cu, and Pb. The data were measured in the forward spectrometer/target calorimeter detectors of the E814 apparatus. The results indicate the existence of two distinct domains, one of beam rapidity projectilelike nucleons, and the second of participant nucleons. From the former, the in-medium inelastic nucleon-nucleon cross section is deduced. It is found to agree, within 10% with the "free" value of 30 mb although under present conditions one of the two colliding nucleons has been struck before with a high probability. We compare with the present data the predictions of a fragmentation model as well as of models dealing explicitly with the heavy-ion collision and particle creation and emission.

PACS number(s): 25.75.+r

I. INTRODUCTION

Hot and dense nuclear matter may be formed when two nuclei collide with each other at relativistic energies. If high enough energy and/or baryon densities are achieved, the formation of a quark-gluon plasma is expected. In the present fixed target experiments, the critical contours in the density-temperature phase diagram can most likely be studied at moderate temperature ($T > 0.15$ GeV) and baryon density several times that of nuclei in their ground state. For a survey of the present theoretical status see Jacob's contribution [1] to *Quark Matter '88*, e.g., and references therein.

Since high energy density is considered a prerequisite for quark-gluon plasma formation, it is essential to obtain experimental information that quantifies the amount of energy lost by nuclear projectiles in their passage through target nuclei. While data from proton-nucleus collisions suggest a fairly large rapidity shift of the incident protons [2] (1.5–2 units of rapidity at an incident energy of 100 and 200 GeV), corresponding to a strong reduction in energy, it is not *a priori* clear what to expect for the case of a nucleus-nucleus collision. The basic difference is that projectile and target nucleons undergo multiple collisions and their "stopping power" might be reduced after the first interaction leading to nuclear transparency or enhanced resulting in increased stopping. In the former case nucleus-nucleus collisions would not necessarily lead to substantially increased energy densities as compared to nucleon-nucleus collisions.

A related question is to what extent the energy deposited in the overlap region between target and projectile is actually thermalized and whether we create an equilibrated system. One way to assess the energy deposition and equilibration of the system is to measure the transverse energy E_t over a large fraction of the total solid angle. This quantity is kinematically constrained by the center-of-mass energy. Information about stopping is obtained by comparing experimental data to calculations based on theoretical models. We have performed [3,4] such measurements within experiment 814 and model comparison suggests the need for a large degree of stopping. A recent survey of the results of such global variable measurements is given in Ref. [5]. In this paper, in order to explore energy loss and stopping, we will use the complementary and more direct method of measuring distribu-

 ©1992 The American Physical Society

tions of leading baryons, protons and neutrons, as a function of centrality of the nuclear collision.

An understanding of equilibration and thermalization requires information about the rapidity densities and transverse momentum distributions of nucleons over the whole range of rapidities and transverse momenta. Experiment 802 has published [6] proton rapidity densities at and backwards of midrapidity, i.e., from $y=0.6$ to 2.0, for 14.6 GeV/nucleon Si+Au collisions and transverse momenta $p_t > 0.4$ GeV/c. Experiment 810 has obtained [7], as the difference of distributions of positively and negatively charged tracks in a time projection chamber, spectra that are assumed to represent proton distributions. In this paper we will present complementary information for protons and neutrons for rapidities above 1.6 and transverse momenta from 0.0 to 0.35 GeV/c. This acceptance provides rather complete coverage for projectile fragmentation products and some, although limited, coverage for participant nucleons. For such nucleons the present E814 acceptance does not allow the measurement of p_t integrated rapidity densities. However, our measurements provide reliable information on particle yields near $p_t=0$. Such data are directly amenable to model comparisons and constrain predictions of rapidity densities in the stated range.

Section II describes the experimental arrangement and the procedural details of the data collection and analysis. This is followed in Sec. III by a detailed discussion of the rapidity and transverse momentum data. Section IV discusses the predictions of a simple fragmentation model, a fireball model, and the model HIJET that includes fragmentation, participant nucleons, and produced particles. The calculations, when compared with the data, show clear evidence for the presence of two distinct origins for the detected particles: one of projectilelike nucleons and the other of participant nucleons.

II. MEASUREMENT OF BARYONS IN THE E814 FORWARD SPECTROMETER

A. Experimental setup

The general layout of experiment 814 at the Brookhaven Alternating Gradient Synchrotron (AGS) is shown in Fig. 1. The experiment consists of calorimetry covering nearly the full solid angle, a charged particle multiplicity detector, and a forward spectrometer. Energy flow is measured in the target and participant calorimeters (TCAL and PCAL, respectively). The TCAL consists of 992 NaI crystals arranged in five walls surrounding the target. It covers, with its side walls, a range, on average, of $48^\circ < \theta_{\rm lab} < 118^\circ$ corresponding to a pseudorapidity coverage of $-0.5 < \eta < 0.8$, and, using the back wall, $-2.0 < \eta < 0.9$. The PCAL is a Pb/scintillator sampling calorimeter and covers $1.0 < \eta < 4.0$. This detector was not used in the analysis presented here. Charged particle multiplicity is measured in two disk-shaped silicon detectors (MULT) each with 512 pixels, the combined coverage of which is $0.85 < \eta < 3.8$. Our data on transverse energy E_t production in the TCAL and charged particle multiplicity N_c have been presented

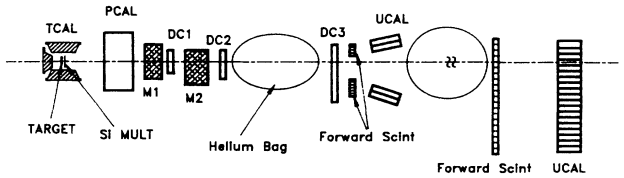

FIG. 1. Schematic outline of the E814 experimental setup in 1989.

elsewhere [3,4]. For the present analysis they are used as measures of the various levels of centrality in the collision. A rectangular hole in the PCAL of dimensions $\Delta x=6.4$ cm and $\Delta y=4.1$ cm determines the acceptance for particles tracked in the forward spectrometer. The coordinate system we use is right handed with the z axis pointing in the beam direction and the y axis in the vertical direction pointing upwards. The target is at the origin of this coordinate system and the TCAL is centered about this origin in x, y with the η coverage given above. The PCAL is centered at $z=122$ cm, i.e., downstream of the target, and is 96 cm deep. This leads to acceptance angles in the spectrometer of $|\theta_x| \le 18.7$ mrad and $|\theta_y| \le 12.0$ mrad.

The forward spectrometer consists of two dipole magnets with a combined maximum $\int B\,dL$ of 6 T m, a set of tracking chambers (DC1, DC2, DC3), a scintillator hodoscope (FSCI), and a set of 25 U/Cu/scintillator sampling calorimeters (UCAL). The overall length of the forward spectrometer is 36.3 m from the target to the front face of the UCAL. The magnet centers are located at $z=3.10$ and 5.29 m, respectively, and have a combined effective bending center at $z=4.54$ m. For the data presented here the field setting was 1.19 T m corresponding to a p_t kick due to the magnetic field of $\Delta p_t=0.36$ GeV/c in the horizontal bend plane (x, z). The three tracking chambers are located at $z=3.98$, 6.90, and 11.59 m, respectively. DC2 has an active area of $\Delta x \times \Delta y = 80 \times 30$ cm^2. It is centered vertically at $y=0$, and horizontally at $x=-20.5$ cm in order to maximize the acceptance for positively charged particles. DC3 has an active area of $\Delta x \times \Delta y = 200 \times 50$ cm^2. It is centered vertically at $y=0$, and horizontally at $x=-51.0$ cm. The tracking chamber between the two magnets, DC1, was not available for the data analysis presented here. The tracking system is described in more detail in Sec. II D.

The FSCI and UCAL have an upstream and a downstream section. The upstream scintillator hodoscope is located, after the last tracking chamber, at $z=12.11$ m backed by UCAL modules at 12.67 m covering, in the bend plane, angles of $\theta_x=19-51$ and $75-108$ mrad to the left and right of the z axis, respectively. Note that the magnetic field deflects positively charged particles to the right, in negative x direction. The region in between $\theta_x=19$ mrad to the left and $\theta_x=75$ mrad to the right is covered by the downstream section of the FSCI at $z=31.3$ m and the UCAL at 36.3 m. The FSCI are vertical plastic scintillator slats (BC404) of dimensions $\Delta x \times \Delta y \times \Delta z = 10 \times 120 \times 1$ cm^3 read out on both ends with photomultipliers (EMI-9954B). Typically, a time

resolution of 300 ps standard deviation is achieved. The gains were chosen such that a minimum ionizing signal is separated about five standard deviations from the pedestal. This also gives good separation from a twice minimum ionizing signal, which would be typical for a double hit. The position of a hit in the vertical direction is determined from both the pulse height measured at both ends of each scintillator and the time difference of the two read outs. The resolution obtained by the two methods is found to be comparable and is typically 3 cm (sigma). The UCAL has been described in Ref. [8]. It consists of 25 modules with an active area of $\Delta x \times \Delta y = 20 \times 120$ cm^2 each and a depth of 4.2 interaction lengths. Each module is divided into 12 optically decoupled towers of $\Delta x \times \Delta y = 20 \times 10$ cm^2 read out on the left and right via wavelength shifter bars and photomultiplier tubes. As outlined in Ref. [8] the position resolution for an isolated hit (cluster) of 12 GeV is $\sigma_x = 1.3$ cm horizontally and $\sigma_y = 1.8$ cm vertically.

B. Data taking

In this paper we present data obtained in a run at the Brookhaven National Laboratory AGS in June 1989 using beams of ^{28}Si at $E_{\rm lab}/A = 14.6$ GeV and targets of natural Al, Cu, and Pb. The areal densities of the three targets were 0.33, 0.60, and 1.18 g/cm^2 corresponding to 1.2% of a nuclear interaction length for silicon. Typical beam intensities were $5 \times 10^4 - 1 \times 10^5$ particles per 1 sec AGS spill. Data were accumulated for each target for about 13 h corresponding to a total of about 6×10^8 beam particles. The typical computer live time was 78%, leading to an integrated luminosity per target of $2-5/\mu$b.

Data were accumulated using a mix of triggers at different levels of centrality. In addition, there were pretriggers equivalent to minimum bias interaction triggers, beam triggers, and random triggers. The centrality triggers were derived from the transverse energy measured in the TCAL or the charged particle multiplicity measured in the MULT. Both types of triggers require a pretrigger consisting of either a small number of hits in MULT (15) or ≥ 4 hits in the scintillator paddles lining the inside of the TCAL. Level 1 of the trigger allows for a possibility to veto events if a second beam particle follows the original pretrigger within 1 μs. Level 2 of the trigger uses information from a FERA system and occurs approximately 10 μs after the pretrigger. For the TCAL, part of the signal from each channel in the side walls is used to form analog sums. Each signal is given a resistive weight corresponding to the sine of the angle with respect to the beam direction of the respective detector element. The weighted signals of two rows of crystals (rows of 13 crystals running in z direction) are added using resistors. These analog sums, which are proportional to the E_t measured in sections of the TCAL, are then digitized in a FERA system. Similarly the raw hit multiplicity in MULT is encoded and digitized. For each target appropriate software thresholds are set on the digitized FERA information to form the level-2 triggers at different levels of centrality. Note that TCAL triggers correspond to E_t measured in the backward hemisphere in the center-of-mass (c.m.) frame, while MULT triggers are sensitive to charged multiplicity at and forward of midrapidity. For both TCAL and MULT there were three different levels of centrality. For the Pb target they were set at 0.2%, 3%, and 17% of the reaction cross section and values for the other two targets were similar. All but the most central level of the TCAL and MULT triggers were downscaled appropriately to cover the whole impact parameter range with comparable statistics. The random triggers serve for monitoring purposes, e.g., of noise and pedestals. In addition, events were accumulated using a empty target frame. They are used for background subtraction and, more specifically, to identify and subtract events due to interactions upstream of the target. Such events are a minor background for multiplicity triggers and generally more important for the E_t triggers. For a quantitative discussion see below.

Valid beam particles are defined by a sequence of scintillators located 1.8–6.5 m upstream of the target. The beam defining system consists of two small disks (1.8 and 0.9 cm diameter and 0.5 mm thickness) 4.2 m apart, where a pulse height consistent with a charge 14 particle is required. Each is backed by a larger scintillator (15 cm diameter and 1 cm thick) with 1.5 and 0.6 cm diameter holes, respectively, in their centers, where signals with pulse heights equivalent to minimum ionizing particles or larger are vetoed with $>90\%$ efficiency. This beam definition typically accepts 25–40 % of all beam particles and leads to a beam spot of about 4 mm diameter at the target with a divergence of about 1 mr horizontally and 2 mr vertically. The second small scintillator also provides the time-zero signal for the time-of-flight measurement and has a time resolution of 100 ps standard deviation. The timing counter is made of BC402 scintillator and is read out with Hamamatsu R2083 photomultipliers. Signals above minimum ionizing in any of the four scintillators are used to derive the level-1 veto discussed in the previous paragraph.

On the event level there are three sources of background for moderately central to central collisions.

(i) Multiple beam particles. In spite of the level-1 veto on this occurrence there is still a small number of events (about 1–2 %), in which a second beam particle arrived too close in time to the first one to be vetoed. Such events are easily visible due to the doubled pulse height in the beam defining scintillators and they are rejected off-line.

(ii) TCAL E_t triggers are rather sensitive to upstream interactions since the trigger levels correspond to relatively low energies (5–15 GeV) due to the kinematic region covered by this detector. This trigger level can easily be exceeded by even a single nucleon hitting the detector from an upstream direction. Such upstream interactions need to be vetoed online. The majority is rejected by a simultaneous requirement of E_t in the TCAL and some minimum multiplicity from MULT. This can be done without biasing the event sample for intermediate to high E_t, where one is most sensitive to this type of background. The remaining upstream interactions are rejected off-line using the correlation of energy in the TCAL back wall with energy in the side walls. For the lowest

transverse energies of less than about 1 GeV in the TCAL remaining background is removed by subtracting cross sections obtained from runs with the empty target frame only. Typically, 5%, 15%, and 50% of the events are rejected off-line for the Pb, Cu, and Al targets, respectively.

(iii) Pretriggers due to delta-rays. Since the pretrigger conditions are set to be very loose, there is about a 50% chance that they are satisfied by delta rays generated by the beam traversing the target. Typically there are about three and five delta rays into the acceptance of the TCAL and MULT, respectively, for Si on a Pb target. Again, such events are easily recognizable off-line by inspecting the pulse height in the downstream FSCI typically hit by the beam. If it exceeds a certain level, indicating that a beam particle is still present, this pretrigger event is rejected.

C. Neutron measurement

Neutrons are measured in six modules of the UCAL 36 m downstream of the target. These six modules are centered about the 0° line (z axis) and cover ± 60 cm vertically and ± 63.2 cm horizontally. In the vertical direction the collimation due to the opening in the PCAL confines showers to be well within the calorimeter boundaries since particles hit only within ± 46 cm i.e., 14 cm or more from the physical boundary of the calorimeter. In the horizontal direction we impose a software cut to confine showers to $-50 \leq x \leq 50$ cm, i.e., a distance of 10 cm or more away from the physical edges of the outermost calorimeter modules in the x direction. The region in p_t and y where neutrons are accepted, due to collimation and software cuts, is indicated by the dotted line in Fig. 2 (left panel). Neutrons are accepted to the right of this line. The acceptance shown is the result of a simulation using the GEANT package [9] after implementation of the full geometry of E814. Since the collimator is rectangular in shape and not round, the acceptance drops below 100% for a given rapidity at a somewhat lower transverse momentum as indicated by the line marked with diamonds in Fig. 2. Events with neutrons in the p_t range between this line and the dotted line can be corrected for the loss in acceptance, while there are no neutrons detected in the y,p_t range above and to the left of the dotted line. The necessary correction factors $1/\epsilon(y,p_t)$ are provided by the GEANT simulation and examples are shown in the right-hand panel of Fig. 2 for protons (see below) in three different rapidity bins. The factors for neutrons are very similar. In the following, data will be presented only in the range where the correction factor does not exceed the value of 5. Over most of the p_t range shown, the correction factors are close to 1.

A neutron is identified as a cluster of energy E in the UCAL neutron acceptance region with no signal in the corresponding region of the FSCI hodoscope in front of the calorimeters. Pulse height signals in the UCAL are analyzed using a cluster algorithm described in more detail in Ref. [8]. The algorithm starts from local maxima in pulse height, corresponding in the present analysis to an energy of 1.5 GeV or more in one 10×20 cm^2 tower. After inspecting the surrounding towers it then finds the total energy in a cluster and the position of the cluster in x and y. Local maxima are required to be separated by at least one tower with a lower pulse height. Merging clusters are disentangled using measured and simulated shower profiles [8] and energy in the overlap region is

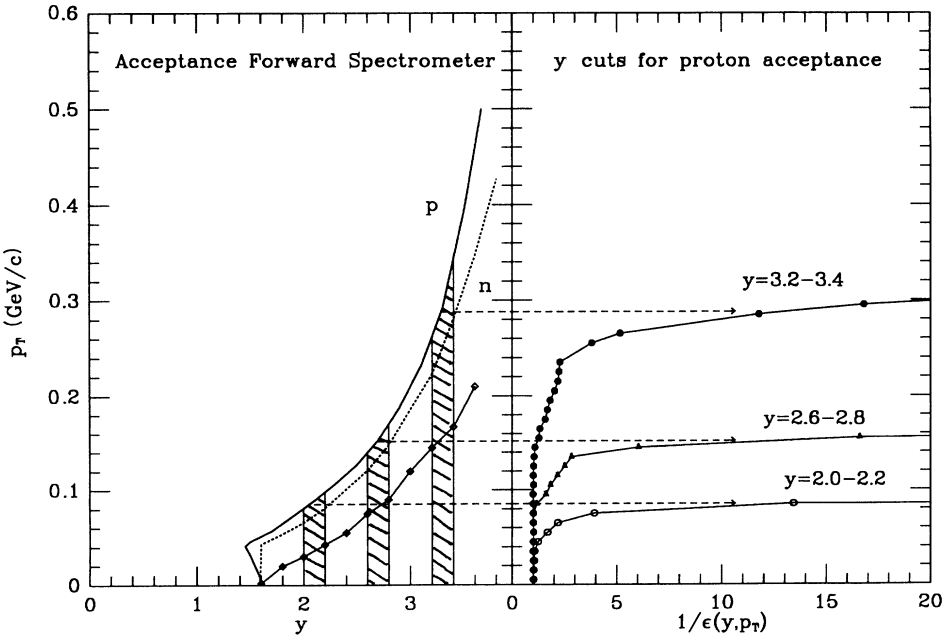

FIG. 2. Left: Acceptance in a p_t vs y plot for protons and neutrons (solid and dotted lines, respectively). The solid line with diamonds marks the p_t values, where the acceptance drops below 100%. Right: Acceptance correction factors for three selected rapidity bins, indicated as hatched areas in left panel, as a function of p_t for protons.

shared appropriately. We find that merging clusters of 13.6 GeV, for instance, need to be separated by 8 cm or more to be identified as more than one hit. The threshold in the local maximum implies that no clusters below 1.5 GeV are found and clusters with energies less than about 3 GeV have a reduced detection efficiency. Hence the boundary of $y=1.6$, corresponding to a kinetic energy of $T_k=1.5$ GeV, for the neutron acceptance in Fig. 2. On the other hand, due to the fluctuations in a hadronic shower, particles which would fall below a 1.5 GeV threshold according to their incident energy are detected with some probability. The quantitative balance between these two effects depends on the spectrum of incident neutrons. For moderately central and central collisions the two effects are found to nearly cancel, while for more peripheral collisions the loss dominates between $T_k=1.5$ and 3 GeV. We will discuss here only data for $y>2.0$ or $T_k>2.6$ GeV. Data have not been corrected for the finite probability that a neutron does not interact in the calorimeter, either due to the finite depth (1.5% inefficiency) or due to the cracks between modules ($<5\%$).

Since for kinematic reasons there should not be any neutrons with rapidities considerably larger than beam rapidity or kinetic energy larger than 13.6 GeV, clusters above a certain energy $E_{\rm thr}$ are assumed to be due to two hits on top of each other (i.e., within $\Delta r \leq 8$ cm). The value of $E_{\rm thr}$ is determined by the energy resolution for a beam rapidity neutron (see below). We choose a value that is 6.4 GeV above 13.6 GeV, equivalent to three standard deviations. For lack of any better information the cluster algorithm shares the energy between the two overlapping clusters by randomizing about $E/2$ (for $E>E_{\rm thr}$) using a Gaussian distribution with a width equal to the calorimeter energy resolution. As can be seen from the data presented below in central collision such unresolved clusters are a rare occurrence (in the 2–4 % range). For the most peripheral collisions discussed here they represent 13% of the neutron multiplicity, and there the spectrum is strongly dominated by neutrons of beam rapidity so that the assumption of equal energy on average is appropriate.

The energy resolution of a single UCAL module was measured [8] using monoenergetic particles of 5–15 GeV/c. For hits in the center of a module a value of $\sigma_E({\rm GeV})=0.4\sqrt{E}$ (GeV) was found. In the present setup and under average running conditions we typically obtain somewhat worse resolutions, e.g., of 16% at 13.6 GeV. This is due in part to a position dependence of the pulse height, the fact that all channels have a common ADC gate but not exactly the same signal delay, and gain stability in the individual towers over the running period. Cracks between modules and general nonuniformities in the calorimeters also adversely affect the resolution. The noise in an individual channel is dominated by the uranium noise due to radioactivity. It corresponds to an equivalence of <100 MeV and is uncorrelated between channels. The value of 1.5 GeV for a local maximum is well above this noise and in fact not limited by noise at all. It is determined instead by the nature of fluctuations in hadronic showers. For instance, lowering the value to 1.0 GeV leads to a 5% increase in the number of clusters found in the average event. The increase can be traced to spurious low energy showers found in the vicinity of a cluster of 13.6 GeV. Shower simulations reproduce this effect, and although showers of 1 GeV energy or even less are visible if they are isolated, they cannot be admitted in the presence of higher energy showers as this leads to additional spurious clusters.

The observables for a neutral particle detected in the manner described above are kinetic energy (T_k) and position (x,y) of the hit. From these the rapidity and the transverse momentum are computed assuming the particle is a neutron. The position resolution quoted above (Sec. II A) leads to a transverse momentum resolution dominated by the energy resolution. At $p_t=0.005$ GeV/c, the center of the lowest p_t bin discussed below, the position resolution contributes 0.0014 and 0.0086 GeV/c at $y=1.6$ and 3.44, respectively. For the largest transverse momenta at any given rapidity the position resolution contributes 10% to the uncertainty in p_t. Because of the large lever arm of 36 m one has to make sure that the beam is aligned along the 0° line of the setup. A tilt of 1° would lead to a displacement, at the position of the UCAL, of 63 cm thus creating a transverse momentum error of 0.250 GeV/c for a neutron with beam momentum. In practice the actual beam direction is monitored during data analysis and all transverse momenta are calculated relative to it. The sensitivity is very good because of the large lever arm, and displacements of 2 cm, or 0.6 mrad, are detectable and can be corrected for. As mentioned above there is a small but finite divergence of the beam. This does not cause a systematic shift in transverse momentum but does lead to a small yet finite broadening of the spectrum. This effect is largest at beam rapidity (0.015 GeV/c) and within our bin size of 0.010 GeV/c for neutrons with rapidities $y\leq 3$. The effect has been taken into account in the Monte Carlo simulations for the acceptance correction and acceptance corrected p_t spectra.

Background in the neutron sample comes from two sources: (i) Charged particles and (ii) neutrals, chiefly photons and possibly secondary neutrons.

(i) Charged particles are rejected by the FSCI hodoscope. For every cluster found in the UCAL we project back to the FSCI hodoscope in the negative z direction and check whether there was a hit within a region of 20×20 cm^2. The size of this square is determined by the position resolution in both detectors as well as a range of angles of incidence, covering both particles coming from the bend center of the magnets and the target in horizontal and vertical direction, respectively, as well as from downstream interactions. The actual number of vetoed hits depends on the x position as well as on the centrality of the collision. It is very small to the left of the 0° line, where in Si+Pb at intermediate E_t values (see below) about 3% of the clusters are rejected. It rises gradually towards the right-hand edge of the neutron region (to about 15%) as the region of the deflected beam and high momentum protons is approached. For the present data obtained with the relatively low magnetic field (see above) we have in fact not used the right-most neutron module,

which is adjacent to the module hit by the beam. This was taken into account in performing the acceptance correction. A veto would still be possible, but the overlap probability between a neutron and a charged particle is no longer negligible, thus leading to an inefficiency for neutron detection. The fraction of vetoed charged clusters in the neutron region is determined by the number of charged particles entering the forward spectrometer and is therefore both target and E_t dependent. For $E_t=4-8$ GeV, 8%, 13%, and 24% of the clusters are vetoed for the Pb, Cu, and Al targets, respectively. For $E_t=8-10$ GeV and Pb this value drops to 2%.

To obtain the veto efficiency, we estimate that cracks between the scintillator slats amount to at most 2% of the solid angle. The actual efficiency of a scintillator hit by a charged particle is, for the purpose of the present analysis, defined by the probability that TDC signals are present for both photomultiplier tubes. This was tested using charged tracks identified with the tracking chambers and the efficiency is generally around 93%. Considering the number of vetoed charged hits discussed in the previous paragraph, background due to hodoscope inefficiency is not relevant to the present neutron data and their uncertainty.

(ii) Background due to neutral particles is a more difficult question and one has to again distinguish two sources. The rate of photons from the decay of neutral pions can be estimated from our measurement of charged pions and Monte Carlo simulations. Most relevant are photons in the energy range 2.8–5.8 GeV, due to neutral pions in the rapidity range from about 3.0 to 4.5. The basic strategy is to tune a model/event-generator to describe charged pions both at midrapidity, where measurements exist from the experiment 802 Collaboration [6] for rapidities $y=0.7-2.0$, as well as in the very forward range $3.5<y<4.5$ covered by the present E814 acceptance (see Sec. II D below). The same event generator is then used to produce neutral pions and their decay photons are tracked through the E814 forward spectrometer using GEANT [9]. As a result we estimate the following photon background in the Si+Pb neutron data for the highest E_t trigger: $20\pm10\%$ at $y=1.75$, $9\pm4\%$ at $y=2.0$, and $3\pm1\%$ at $y=2.5$. For more peripheral collisions this background is reduced. The uncertainty in this number is systematic due to the use of different types of event generators. The other possible source of neutral particle background in the neutron sample is secondary interactions of particles produced in the target. Such secondary interactions could be due either to particles hitting the PCAL, which acts as the collimator for the forward spectrometer as outlined above, or to particles actually emitted into the spectrometer acceptance and interacting in either the tracking chambers or the gas along their flight paths. We have simulated both effects and find that they are negligible (typically less than 5%) for the data discussed below.

D. Charged particle measurement

The identification and measurement of charged particles in the E814 apparatus is performed using all the elements of the forward spectrometer with the exception of the UCAL. In the present analysis, charged particle tracks are measured in DC2 and DC3, the two drift chambers located downstream from the magnets, and the forward scintillator hodoscope.

The two drift chambers are identical in design and differ in size only. They each contain six wire planes providing a total of 12 x-position measurements at known z values along the track. Each wire plane consists of alternating sense and cathode wires. DC2 has 128 sense wires in each drift plane and DC3 has 160. The sense wires in adjacent planes are displaced with respect to each other by half a cell width to aid in the resolution of the left-right ambiguity in the assignment of the position of a track with respect to each sense wire. The drift cell size, or the distance from sense wire to sense wires, is 6.4 mm in DC2 and 12.7 mm in DC3. The sense wires are made up of gold plated tungsten filament with a diameter of 17.5 μm. Thin wires were chosen to provide gain saturation for large amplitude signals, providing a large dynamic range for the simultaneous detection of minimum ionizing (singly charged) and 200 times minimum ionizing (silicon) particles. The individual drift planes are separated from each other by an anode foil of 25 μm thick aluminized Mylar. These foils serve to both shape the field within the chamber, and to minimize the propagation of delta rays from plane to plane. The chambers are filled with a 50%-50% argon-ethane gas mixture at atmospheric pressure. This gas yields a maximum drift time of 65 ns in DC2 and 130 ns in DC3. The single-point, single-plane position resolution for minimum ionizing particles and for both drift chambers has been determined [10] to be 250 μm using a proton test beam supplied by the AGS. The single wire efficiency for detecting a minimum ionizing particle was determined to be about 90% from the same proton test beam data. Directly behind the wire planes of each drift chamber lies a pad plane, or segmented cathode-read-out detector, capable of providing an additional measurement in x an y. These were not yet implemented for the data described here. For the present data set, the forward scintillators provide the only measurement in y for each charged particle track (see II A).

The information in x from DC2 and DC3 and the x and y information from the FSCI hodoscope are used to reconstruct tracks of charged particles propagating through the spectrometer. The pattern recognition used for the construction of these tracks is based on a depth-first, or "tree," algorithm [11]. The general strategy applied to these data is to begin by finding track segments within each drift chamber. The tree algorithm is desirable in this case since it successfully solves the left-right ambiguity when reconstructing these track segments. Our tree algorithm has been designed to assemble tracks that contain hits in three or more of the six planes within each drift chamber, thus allowing for missing hits or dead wires within the chamber. For the run in 1989, when these chambers were operated for the first time, 6% of the wires in the chambers were not operational and on average a track segment consists of five wire hits. The efficiency for finding a track segment using this algorithm

is very close to 100% as determined from Monte Carlo–generated events and results using the proton beam. The only case where this efficiency actually drops below 100% is when two tracks traverse the chamber within adjacent drift cells of each other. This will be addressed in more detail below. The resulting track segments are stored as two-dimensional line segments that can be projected to any other detector in the spectrometer. In the same manner, hits from the FSCI are stored, providing spatial measurements in x and y along with time-of-flight and charge information.

With track segments constructed in each drift chamber and hits identified in the forward scintillators, the pattern recognition next attempts to connect the information from these detectors into a three-dimensional straight-line track for the region downstream of the magnets. The method applied at this point is again based on the tree algorithm. The algorithm forms "links" between the hits in each of the detectors and then groups the links into tracks using comparison criteria customized for the detectors being linked together. For example, when connecting track segments in DC2 to DC3, one requirement is that the segments must point towards each other, within measured uncertainties. Again, this algorithm handles events in which, in principle, all or part of the information from a detector could be missing. However, for the data presented here, we require that a valid track contain components from DC2, DC3, and a forward scintillator. The efficiency of this step is measured for single tracks to be better than 98%.

Once the tracks are completely constructed downstream of the magnets, they are projected back through the magnets in the bend plane to the target. We use a simple magnetic field model for this projection defined by a uniform dipole field that extends for 7.6 cm beyond the physical boundary of the magnet on each end and drops to zero at this distance. Actual measurement of the magnetic field shows that this simple model is a very good approximation to the actual field integral $\int B\,dL$. Errors introduced by the field model in the calculation of the momentum of the protons are easily within the resolution of the apparatus. The projection through the magnets is done with the assumption that a given track originates from the coordinate system origin at the target. For the present data, the horizontal beam spot size was typically less than 4 mm and the Pb target, for instance, was about 1 mm thick, so the assumption of the track origin introduces an uncertainty of less than 1% in the momentum resolution. This uncertainty does not inhibit the ability to identify protons. Multiple scattering in the target contributes about 1% to the momentum resolution and is therefore the dominant effect.

The overall efficiency of the pattern recognition software for identifying single minimum ionizing tracks is near 100%. This was determined by analyzing data from a monoenergetic proton test beam of 10 GeV/c momentum provided by the AGS. The analysis was done on events where a single proton was traversing the spectrometer. For Si+A events in the present analysis, the average number of charged tracks in the forward spectrometer is about one for the more peripheral collisions and about 0.3 in very central collisions (see below). Even for the most peripheral trigger the probability for three tracks in one event is of the order of 5% only and about one order of magnitude lower for the most central trigger. Therefore, inefficiencies due to overlapping tracks are negligible in this data sample. All proton data presented in the following are corrected for small and known detector and electronic read-out inefficiencies.

After track reconstruction, the particle identification is done by comparison of momentum and velocity. Figure 3 shows for charge 1 particles a scatter plot of the inverse momentum versus the time of flight, calculated relative to a $v=c$ particle. One can easily distinguish the bands due to positive pions, protons, and deuterons as well as a few tritons in this plot. The cluster of points centered about $1/p \simeq 0.03$ c/GeV is due to beam rapidity deuterons. The area enclosed by the solid line indicates those tracks that we classify as protons for the present analysis. The boundary on the low time-of-flight side follows the valley between pions and protons. Some small contamination from pions in this proton gate is due to pions with momenta larger than 7 GeV/c or $y>4.5$, where separation via time of flight is no longer possible. Using our measured π^+ cross section in the rapidity interval 3.5–4.5, pion background underneath beam rapidity protons is estimated to be less than 1%.

From the spatial position of the charged particle track we can determine the angles θ and ϕ under which the particle was emitted from the target. The respective resolutions are $\Delta\theta=0.5$ and $\Delta\phi=1.6$ mrad. The horizontal momentum $p_h=(p_x^2+p_z^2)^{1/2}$ is determined from the track reconstruction as discussed above. Using the horizontal momentum and the emission angles θ and ϕ, the momentum p and the transverse momentum $p_t=(p_x^2+p_y^2)^{1/2}$ are determined. Having identified the particle as a proton by the cut indicated in Fig. 3, the rapidity of the particle is calculated using its momentum and the true rest mass energy as

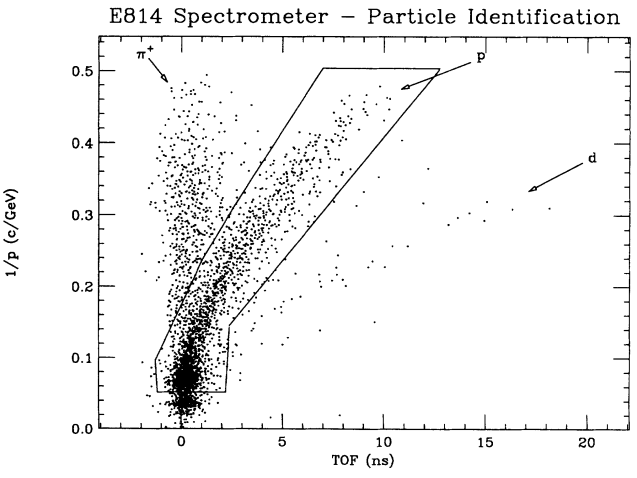

FIG. 3. Particle identification plot of inverse momentum vs time-of-flight difference with respect to a speed of light particle for charge 1 particles from events satisfying any of the three second level E_t triggers.

$y = \cosh^{-1}\{[(m_0c^2)^2+(pc)^2]/[(m_0c^2)^2+(p_tc)^2]\}^{1/2}$.

The region in transverse momentum and rapidity where protons are accepted is shown in Fig. 2 (left panel) and is defined by the size of the PCAL opening, the size of the drift chambers, and the magnetic field. The acceptance for protons in the data presented here was incorporated in the analysis in a manner identical to that described for neutrons above.

Positive pions were analyzed using the same procedure as for protons. In the present geometry E814 accepts pions in the range $y = 3.5-4.5$. The lower limit is given by the magnetic field, which transports particles with momenta greater than 2 GeV/c into the drift chambers; the upper limit is restricted by the particle identification due to time of flight and momentum (see Fig. 3), which in the present setup allows for pion separation from protons only for $p \leq 7$ GeV/c. Only transverse momenta $p_t \leq 0.15$ GeV/c are accepted due to the PCAL collimation, which leads to a multiplicity of only $\langle n_{\pi^+} \rangle = 0.03$ per central collision. This number is used together with data measured [6] at midrapidity by experiment 802 to determine the photon background underneath the neutron sample as outlined in Sec. II C above.

III. RESULTS

A. Rapidity distribution

Figure 4 shows the distributions in rapidity of protons emitted into the acceptance of the forward spectrometer. The data shown here are integrated over the accepted p_t interval for every rapidity bin. Data are shown for Si+Pb collisions and three different levels of centrality defined by transverse energy measured in the TCAL. The three levels of centrality correspond to the three level-2 triggers in TCAL E_t and represent trigger cross sections of 593, 102, and 6.9 mb for the top, middle, and bottom figures, respectively. The data are corrected for background that is not target related by using the runs with an empty target frame. For Si+Al and $E_t = 2-4$ GeV (6–8 GeV) this subtraction amounts to 9% (1%). For Si+Cu at low E_t, it is 3%. For higher centrality and for the Pb target at all centralities, it is completely negligible. The error bars shown reflect the statistical uncertainties. In each spectrum a clear peak of beam rapidity protons is visible. The width is of the order of 0.3 unit of rapidity (FWHM) corresponding to 4.4 GeV/c or 30% in momentum. This is much larger than the momentum resolution in the tracking detectors and is addressed quantitatively in Sec. IV. With increasing centrality, the intensity of this beam rapidity peak decreases markedly. This is illustrated in more detail in the next section. The falloff in cross section towards midrapidity is due to the decreasing acceptance in p_t, as shown in Fig. 2. Very similar data have been obtained for neutrons. Since the corresponding spectra have been published [3] for the run in December 1988, they are not displayed here. For the Al and Cu targets the rapidity distributions for all three E_t triggers look very similar to the top panel of Fig. 4. The relevant quantitative information is displayed in Fig. 5, as discussed in the next section, for all three targets and protons as well as neutrons.

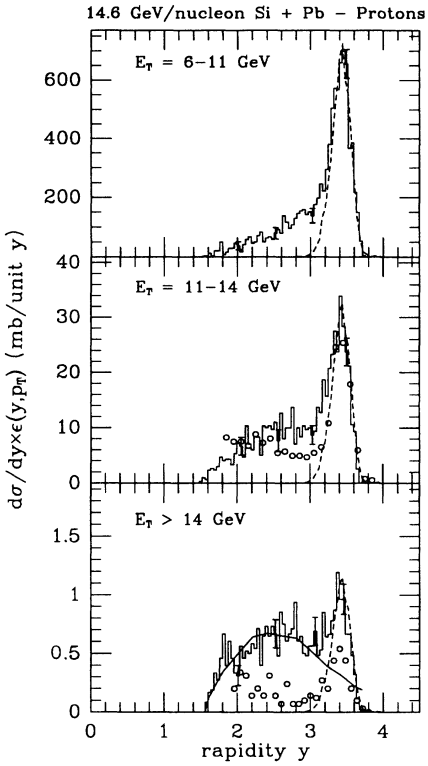

FIG. 4. $d\sigma/dy$ for protons measured in the acceptance of the E814 forward spectrometer for three different cuts on TCAL E_t (see text). Dashed lines: Fragmentation model described in Sec. IV A. Open dots: HIJET with rescattering [17]. Solid line: Landau fireball [19].

B. Multiplicity of beam rapidity nucleons

By generating rapidity distributions for small intervals in E_t, one can quantitatively study the dependence on centrality of the peak of beam rapidity nucleons. We define beam rapidity nucleons as protons and neutrons

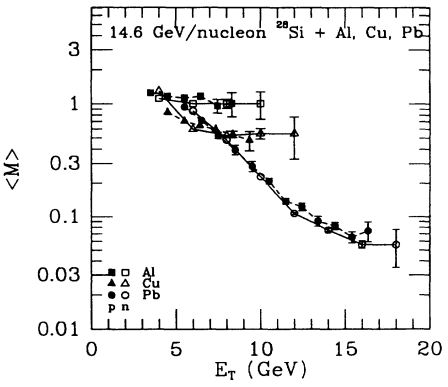

FIG. 5. Average multiplicity of beam rapidity baryons for Si+Al, Cu, and Pb. Solid and open symbols correspond to protons and neutrons, respectively.

with rapidities larger than 3 and p_t values such that they are accepted in the forward spectrometer. There are three criteria that justify the value of the rapidity cut. Inspecting the distributions $d\sigma/dy$ for more central collisions, there appears to be a definite break or even dip in the spectra around that rapidity (see, e.g., bottom of Fig. 4 and also the respective neutron spectra in Ref. [3]). As we discuss in the section on transverse momentum distributions, along with this break in the rapidity spectrum there is, at $y=3$, a change in both the slope and intercept at $p_t=0$ of the invariant cross section as a function of p_t, suggesting a distinction in the nature of forward nucleons emitted at $y<3$ and $y>3$. Furthermore, a calculation based on a fragmentation model (see Sec. IV A) that describes rather well the rapidity and p_t distribution of these beam rapidity nucleons also indicates that this particular source of nucleons vanishes for $y<3$ (see dashed lines in Fig. 4).

Figure 5 shows the multiplicity of the beam rapidity protons and neutrons for the three difference targets, as a function of E_t measured in the TCAL. Again, the error bars shown reflect the statistical uncertainties. The data shown here are not extrapolated to larger p_t values, but rather correspond to the measured range in p_t as indicated in Fig. 2. Extrapolation would be model dependent. Using a fragmentation model (see below) the forward spectrometer acceptance for beam rapidity nucleons is about 71%.

From Fig. 5 two trends are obvious.

(i) For central collisions the multiplicity, $\langle M \rangle$, of beam rapidity nucleons decreases rapidly with increasing target mass. For each target the highest E_t bin shown in Fig. 5 corresponds to $<0.002\%$ of the geometric cross section, σ_{geo}. Assuming impact parameter and cross section are related by the simple equation $\sigma=\pi b^2$, this would correspond to impact parameters $b<0.05$ fm. Of course there are fluctuations about this number and we will only assume in the following that the highest E_t bin corresponds to collisions with full overlap between target and projectile. The values of $\langle M \rangle$ for these very central collisions can be interpreted as the transparency of Al, Cu, and Pb for 14.6 GeV/c nucleons in a Si projectile and we will discuss this further in IV A.

(ii) $\langle M \rangle$ decreases, for a given target, with increasing centrality. This trend is very pronounced for the Pb target where the E_t bins shown cover a relatively large range of impact parameters. There, the low-E_t end represents 20% of σ_{geo} as compared to 0.002% at the high end. Over this range a decrease in $\langle M \rangle$ by about a factor of 20 is observed. Using standard event generators (see below) as guidance, this cross-section range corresponds to an impact parameter range of 5–7 fm for the lowest E_t value and $b<2$ fm for the highest E_t bin in Si+Pb. For Si+Pb collisions with 5–7 fm impact parameter 1.5–2 protons and neutrons from the projectile survive without any collision, not far from the number actually observed. For the Cu and Al targets $\langle M \rangle$ falls with increasing E_t, but only rather slightly over the interval covered. It should be noted, however, that a given value of E_t corresponds to very different centrality for different targets. So, although the Al data have been analyzed for $E_t>3$ GeV (a lower value than used for the Pb target) this nevertheless represents only 2.7% of σ_{geo}. This explains qualitatively that for relatively low E_t values $\langle M \rangle$ is approximately the same for all three targets.

The agreement between the neutron and proton measurement is remarkably close, considering that the results shown correspond to essentially independent measurements of absolute cross sections. The experimental technique and the detectors involved are different as are the resolutions, backgrounds, and inefficiencies. Closer inspection indicates that on average the neutron multiplicities are slightly below the proton multiplicities as is visible, e.g, in the Pb curve in Fig. 5. This is due to the different energy resolution for protons and neutrons, determined from tracking and calorimetry, respectively. Integrating above a fixed threshold (8.5 GeV in the case of beam rapidity nucleons) yields slightly lower results for the particle measured with poorer resolution.

C. Correlations between forward baryons

In order to study whether the baryons observed in the E814 forward spectrometer are emitted statistically independent of each other or whether there is indication for any correlated emission, we plot in Fig. 6 the probability $P(n)$ to find, in our acceptance, n protons with rapidity above 3. The data shown for Si+Pb cover $n=0$–4 and are displayed again for the three different levels of centrality. Statistical error bars are shown whenever they exceed the size of the symbols. To guide the eye, the experimental points are connected by solid lines. As seen in Fig. 5, with increasing centrality the proton multiplicity decreases and, consequently, the $P(n)$ curves narrow. The three levels of centrality correspond to mean proton multiplicities of 0.43, 0.12, and 0.067. Also shown, as the dashed lines, are Poisson distributions that have, for each level of centrality, the same $P(0)$ as the data and, hence, the same mean proton multiplicity. For the lowest cen-

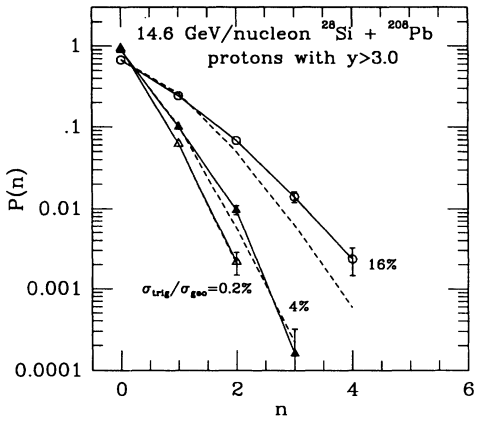

FIG. 6. Probability distribution to find n protons per event for three different levels of centrality obtained by triggering on the TCAL. Data points are connected by solid lines. Also shown as dashed lines are Poisson distributions with the same mean as data.

trality, the data are somewhat broader than a Poisson distribution and the effect appears to be statistically significant. This may be due to the averaging over a relatively large impact parameter range for a low E_t trigger. For the mid- and high-E_t triggers, where in a simple geometrical picture there is complete overlap between target and projectile, the present data agree with statistically independent emission.

D. Transverse momentum distributions

Within the acceptance indicated in Fig. 2, transverse momentum distributions have been obtained for protons and neutrons for all three targets. A typical spectrum $(d\sigma/dp_t)\epsilon(y,p_t)$ for beam rapidity neutrons ($y>3.0$) is shown in Fig. 7. The histogram represents the experimental neutron distribution for Si+Pb and $E_t=11-14$ GeV (102 mb trigger cross section). Note that the most probable transverse momentum is rather low at about 0.1 GeV/c. This result is not an artifact of the limited p_t acceptance of the present experiment. In the bottom of Fig. 7 the inverse acceptance is given and one can see that it is 1.0 or very close to 1.0 for $p_t \leq 0.18$ GeV/c. This acceptance is integrated over the region $y=3.0-3.8$ and based on the shape of $d\sigma/dy$ as found experimentally for this interval and trigger. Comparing the corresponding spectra for the low and high E_t triggers, no significant difference is observed. The corresponding spectrum for protons as well as the spectra for other targets look very similar.

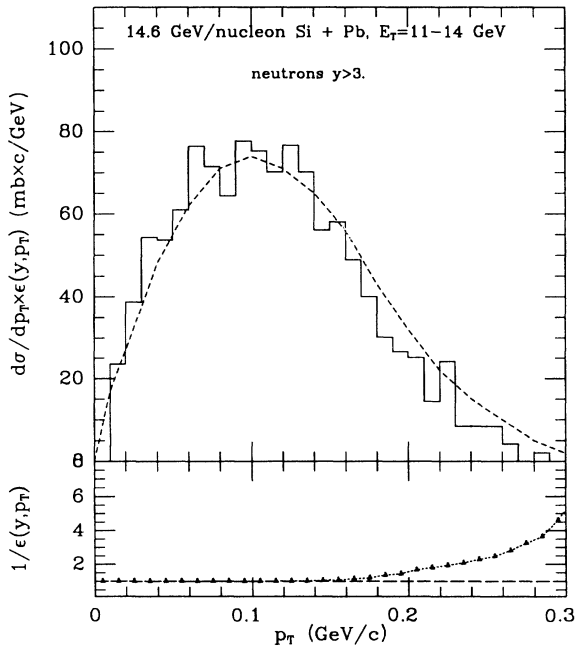

FIG. 7. $d\sigma/dp_t$ into the acceptance of the forward spectrometer for neutrons of $y>3$ in Si+Pb collisions (histogram) and for same trigger condition as central panel in Fig. 4. Dashed line: Result of Goldhaber fragmentation model [13] and $p_F=0.27$ GeV/c. Bottom panel: inverse spectrometer acceptance as a function of p_t.

In Fig. 8 we display transverse momentum spectra for different rapidity intervals and the intermediate centrality E_t trigger ($\sigma_{trig}=141$ mb). The vertical axis of the plot is $2\pi\sigma_{inv}=1/p_t\, d^2\sigma/dp_t dy$. Each curve corresponds to a rapidity interval of 0.2 unit width, starting with $y=2.0-2.2$ as the bottom curve and ending with $y=3.6-3.8$ at the top. Since the invariant cross-section levels are very similar for all rapidities, the data were multiplied by increasing powers of 5, as indicated in the figure. Data displayed in Fig. 8 have been corrected for acceptance within the p_t range shown. The first bin from 0.0 to 0.01 GeV/c is not shown because of very limited statistics due to decreasing phase space. For each curve typical statistical errors are shown. All curves are very flat and compatible with zero slope at p_t less than about 0.06 GeV/c. For the lower rapidities the p_t range is too limited to exhibit sensitivity to an inverse slope constant. For rapidities of $y>3$, we have fitted thermal distributions of the type $\sigma_{inv} \propto m_t \exp(-m_t/T)$ to the data and very low apparent temperatures of about 7 MeV are obtained. To illustrate this we show, for the rapidity interval $y=3.4-3.6$, curves using $T=150$, 10, and 5 MeV represented by the dashed, solid, and long dashed lines. At rapidities below 3 the data are consistent with inverse slope constants $T \geq 100$ MeV and are certainly in line with values in the 150–200 MeV range as obtained by other heavy-ion experiments [6,7] at the AGS (see dashed line for the $y=2.6-2.8$ bin).

While the p_t range covered by the present E814 acceptance is too small to extrapolate to obtain rapidity densities, except for rapidities larger than 3, we can obtain intercepts of the p_t spectra at $p_t=0$. After dividing by the

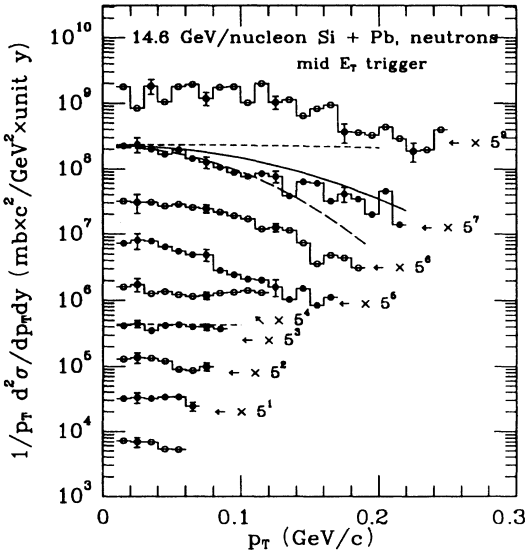

FIG. 8. $1/p_t\, d^2\sigma/dp_t dy$ for neutrons in 0.2 unit y bins for Si+Pb collisions and mid-E_t trigger (143 mb). The bottom curve corresponds to $y=2.0-2.2$, the top curve to $y=3.6-3.8$. For increasing y bins, data are multiplied by increasing powers of 5 for clarity of the picture. Dashed, solid, and long dashed lines: thermal spectra with $T=0.150$, 0.010, and 0.005 GeV, respectively.

trigger cross section they correspond to rapidity densities for protons and neutrons at $p_t = 0$. This quantity should be easily comparable to model calculations and does not require modeling of the acceptance. In Fig. 9 the results for protons and neutrons are displayed for the three targets used. The open symbols connected by the dotted lines correspond to protons, the solid symbols and solid lines to neutrons. As can be seen from the data displayed in Fig. 8 for the Pb target, statistical errors of these intercepts are small, typically of the order of the size of the data points in Fig. 9. There is, however, a systematic uncertainty due to the fit function and range used for the different rapidity bins. We have studied the dependence of the data shown in Fig. 9 on the exact fit procedure and estimate systematic errors to be 10–15 %. The results in Fig. 9 are for $y < 3$ based on a thermal spectral as fit function and for $y > 3$ on a spectrum as due to projectile fragmentation (see below). The data correspond to the intermediate E_t triggers and thus to about 4% of the geometric cross section for each projectile-target combination. One can see a clear peak at beam rapidity. As expected it is largest for Al and smallest for Pb. It should be noted, however, that this does not imply a peak in the p_t integrated rapidity density due to projectile fragmentation. The peak structure observed is largely due to the much steeper slope for projectile fragmentation nucleons. Below this peak and towards midrapidity, the values rise gradually by a factor of 5 for Pb and by a factor of 1.5–2 for Cu. For Al the values are rather flat. The results for protons and neutrons are very close, although the beam rapidity peak for protons is narrower due to the better resolution. For the Pb target and the region below the beam rapidity peak, there is a clear excess of neutrons over protons by about a factor of 4:3. This may reflect the neutron to proton ratio in the Si+Pb overlapping participant volume of 63:46. It should be noted that, since the same fit procedure was used for protons and neutrons, the systematic error quoted above does not affect much this difference between proton and neutron results for the Pb target and $y < 3$.

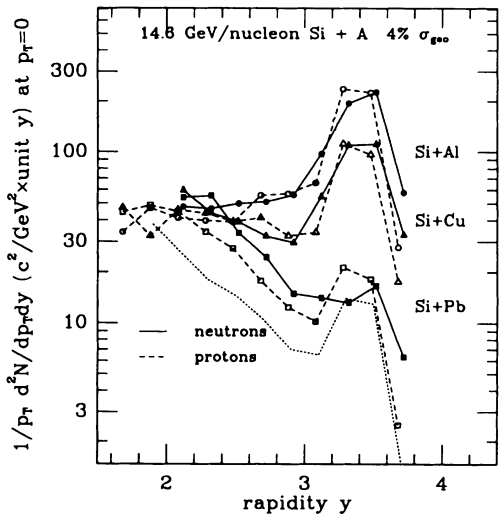

FIG. 9. Rapidity density at $p_t = 0$ of protons (open symbols and dashed lines) and neutrons (full symbols and solid lines) for Si+Al, Cu, and Pb (circles, triangles, and squares, respectively). For clarity of the picture, neutron points are displayed 0.02 unit of y above the center of each rapidity bin, protons points 0.02 unit below. The data points are connected to guide the eye. Systematic errors dominate and are estimated to be less than 15% (see text). Dotted line: from a simulation using HIJET with rescattering [17] for protons from Si+Pb collisions.

IV. DISCUSSION

In the following we distinguish between spectator or fragmentation nucleons and nucleons that have interacted via inelastic collisions. While this distinction is easily possible on a theoretical level, it is less clear experimentally. We use as criteria for the spectator category the existence of a clear peak at beam rapidity and a very low inverse slope constant in the corresponding transverse momentum spectra. For protons this implies that spectators dominate in the rapidity range $y \geq 3.2$, for neutrons the break occurs at $y \geq 3.0$ due to the calorimeter energy resolution. In any case, this cut in rapidity does not give a precise distinction between spectator and participant nucleons; underneath the spectator nucleons there is a tail of nucleons that have actually interacted, with their relative abundance depending on centrality.

A. Beam rapidity nucleons

Nucleons that have not undergone direct inelastic collisions but are emitted from the excited projectile spectator matter should be emitted isotropically in the projectile rest frame with a momentum distribution characteristic for bound nucleons in a nucleus. This question was first addressed by Feshbach and Huang [12] and, generalizing it to fragments of different mass, by Goldhaber [13]. Although the discussion was originally centered around Bevalac data in the 1 GeV/nucleon beam energy range, the same arguments should apply for fragmentation at much higher beam energies.

The momentum distribution of nucleons inside a nucleus is characterized by the Fermi momentum, p_F, and the expectation value of the three-vector momentum is given by

$$\langle p^2 \rangle = 3p_F{}^2/5 \ .$$

Following Ref. [13], we assume for projectile fragments with mass number $A = 1$, or nucleons,

$$d\sigma/dp \propto \exp(-p^2/2\sigma^2) = \exp(-5p^2/2p_F{}^2)$$

using $\sigma^2 = \langle p^2 \rangle /3$. In a Monte Carlo simulation, we have sampled this distribution for protons and neutrons generating rapidity and transverse momentum distributions. In order to make them comparable to the experimental data, the results of the Monte Carlo simulation have been tracked through the experimental acceptance using GEANT and have been convoluted with the experimental resolutions. Note that the normalization in this comparison is arbitrary. The distribution of nucleon momenta in a nucleus has been determined from measurements of high momentum transfer inelastic electron

scattering [14]. For nuclei near Si, the resulting distribution is approximately Gaussian with a standard deviation of 0.235 GeV/c. Huang and Feshbach use 0.23 GeV/c to describe fragmentation of oxygen projectiles at 1 GeV/nucleon beam energy while more recent Bevalac data [15] have been analyzed within the framework of Ref. [13] with values of p_F of 0.19 GeV/c. We left p_F as a free fit parameter and obtained best agreement with the measured rapidity distributions shown in Fig. 4 as well as in Fig. 3 of Ref. [3] for a value of $p_F=0.27$ GeV/c. The dashed lines in Fig. 4 represent this calculation. The value of p_F used is somewhat above that determined for Si from electron scattering.

In order to further test the fragmentation hypothesis one can also compare the transverse momentum spectrum of nucleons above rapidity 3 to the fragmentation calculation for the same Fermi momentum. The result is shown in Fig. 7 as the dashed line. The agreement with the experimental data is very good. A thermal distribution of the type $1/p_t\, d^2\sigma/dp_t dy \propto m_t \exp(-m_t/T)$ would yield a temperature of about 0.007 GeV but the agreement in shape is not as close to the data (see solid and long dashed lines in Fig. 8). The fact that the distributions in rapidity and p_t do not depend significantly on centrality of the collision and the target nucleus give support to the fragmentation hypothesis. It is interesting to note that our deduced p_F values are closer to those determined from electron scattering than what was obtained in Bevalac experiments [15].

We now use the spectral distributions of these beam rapidity nucleons and their agreement with a simple fragmentation picture as an indication that these nucleons have not undergone inelastic collisions. One can then use the probability that such nucleons are observed to extract information about the effective nucleon mean free path or the inelastic in-medium nucleon-nucleon cross section, σ_{NN^*}. In order to come to quantitative comparisons with calculations one has to make the attempt to separate spectator nucleons from nucleons that have interacted but are emitted at rapidities larger than 3, in the experimental data. It is clear from Fig. 4 that, in particular for central collisions, this background is not negligible. Since the fragmentation peak is nearly symmetric about beam rapidity (see dashed lines in Fig. 4) and the fit from the fragmentation model agrees well with the upper half of the experimentally observed peak, we will use, for the following discussion, a corrected multiplicity M_c of fragmentation nucleons rather than the raw multiplicity M_r of nucleons above rapidity 3 and into the experimental acceptance. To this end we first define M_f as twice the multiplicity of protons with rapidity $y \geq 3.44$. The corrected multiplicity M_c is then obtained by dividing out the experimental acceptance, i.e., $M_c = M_f / \langle \epsilon(y,p_t) \rangle$. The so obtained M_c should be directly comparable to model calculations. In Table I are given the values for the raw multiplicity M_r, the background corrected values M_f, and the acceptance corrected values M_c for the low and high centrality ends for each of the three targets. The column M_r reflects the values shown in Fig. 5. Only statistical errors are given and the fractional error in M_f and M_r is therefore the same.

TABLE I. Multiplicites of forward protons are Si+Al, Cu, and Pb. For each target a value at low and high E_t in the TCAL is given. M_r is the multiplicity for $y \geq 3.0$, M_f is the multiplicity for $y \geq 3.44$ times two, and M_c is M_f after acceptance correction. In parentheses the errors in the last digit(s) are given. They reflect the statistical uncertainty only.

Target	E_t (GeV)	M_r	M_f	M_c
Al	3.5	1.25(5)	1.16(5)	1.40(6)
	8.5	1.02(24)	0.88(21)	1.11(26)
Cu	4.5	0.73(4)	0.63(3)	0.79(4)
	9.5	0.65(9)	0.53(7)	0.66(9)
Pb	5.5	0.95(4)	0.83(3)	1.04(4)
	15.5	0.064(7)	0.039(4)	0.049(5)

Conceptually, there are two sources for beam rapidity nucleons that have not undergone an inelastic collision. In the more peripheral collisions the probability of observing such nucleons is dominated by geometry, i.e., the probability that a nucleon misses the target nucleus altogether. Conversely, in central collisions beam rapidity nucleons may appear as a result of finite nuclear transparency. We therefore choose to look at central collisions for the following arguments. Inspecting the curve for the Pb target in Fig. 5, we would conclude that $E_t > 15$ GeV corresponds to full overlap between target and projectile. The exact impact parameter is not crucial for the argument as long as b is less than about 2 fm. Using sharp surface density distributions for the nucleons in projectile and target we can compute the mean number of collisions $\langle n \rangle$ a projectile nucleon undergoes for this collision geometry in terms of the nuclear density and σ_{NN^*} after properly integrating over the target and projectile size. Note that this probability is frame independent since it contains the product of the target thickness and the density, which scale in proportion to $1/\gamma$ and γ, respectively. The probability that a nucleon does not interact is then given as $P(0)=\exp(-\langle n \rangle)$ and the total multiplicity of beam rapidity neutrons or protons from a silicon projectile is $\langle M \rangle = 14P(0)$. For full overlap, $\langle n \rangle$ is calculated using the values from the column M_c in Table I to be 5.66, 3.06, and 2.53 for the Pb, Cu, and Al targets, respectively. This leads to $\sigma_{NN^*}=28.8\pm0.5$, 28.8 ± 1.8, and 30.8 ± 2.5 mb, respectively. These numbers are rather close to the free NN inelastic cross section at this energy, which is 28 mb (see Ref. [16]). This result is quite surprising. To appreciate it one should note that, in the case of Si+Pb, on average every target nucleon is struck twice and every projectile nucleon interacts more than five times. The above result can be interpreted as an indication that the cross section for collisions between previously struck nucleons is not significantly modified from the free value. We note that this, to our knowledge, is the first direct measurement of an in-medium NN cross section. Obviously, our data are sensitive only on the time scale it takes the projectile to pass through any given plane in the target frame, i.e.,

about 1 fm/c, and excitations that materialize more slowly would not affect our results.

B. Interacting nucleons

Following the definition of spectator nucleons outlined above, we classify all other protons detected in the acceptance of our forward spectrometer as interacting nucleons. The rapidity distributions displayed in Fig. 4 have been compared to calculations within two different models. We will first discuss results from a calculation using HIJET with rescattering [17]. This model describes the global observables such as E_t measured [3] in the TCAL and charged particles measured [4] in MULT rather well for all three targets. The open dots in Fig. 4 are results for protons into the acceptance of the forward spectrometer. Clearly, the contribution from interacting protons is underpredicted at these forward angles. At rapidity 2.8–3.0, the discrepancy is about a factor of 2 at intermediate E_t and a factor 3–4 at high E_t. The peak of beam rapidity protons is also less than observed experimentally. Considering that this peak of noninteracting nucleons should sit on a pedestal of interacting nucleons about a factor of 2–3 higher than HIJET predicts, the amount of transparency is not far from our experimental observation. About one of 300 incident nucleons is transmitted without interacting in a central Si+Pb collision. This is consistent with the fact that HIJET uses the pp inelastic cross section for all nucleon-nucleon collisions (see discussion in IV A). Consequently, the fact that interacting protons are underpredicted into our acceptance must mean that they are overpredicted at midrapidity. This may imply that the HIJET parametrization produces too large a rapidity shift for each nucleon-nucleon collision, resulting in proton rapidity distributions that are too narrow compared to the data. However, one should remember that, using HIJET, one reproduces the measured transverse energy and pseudorapidity distributions quite well, which presumably are also sensitive to the amount of NN rapidity shift in each collision.

Another scenario describing most of the data is obtained within the Landau fireball model [19]. Using this approach we have calculated the rapidity distribution of protons within the acceptance of the forward spectrometer. The parameters used are the same as given in Ref. [19], in particular, full stopping is assumed. In contrast to the results of the HIJET simulation, the distributions obtained from a longitudinally expanding fireball reproduce well the experimentally obtained distribution of interacting protons. Note that an isotropic fireball does not give good agreement with the same data (see calculation shown in Ref. [3]). Since this model has no transparency, there is no beam rapidity peak from this calculation. Comparing the HIJET and Landau fireball calculations to the high E_t data, it is indeed suggestive that the fireball scenario with the small but finite transparency would describe our data well. Note that this amount of transparency is so small (the beam rapidity peak contains only about 0.3% of the projectile kinetic energy) that it should not otherwise affect the kinematics, excitation energy, or temperature of the fireball.

The rapidity densities at $p_t=0$ have also been generated using HIJET with rescattering and are shown for protons from Si+Pb collisions as the dotted line in Fig 9. While the overall shape of the data is reproduced, the $p_t=0$ proton rapidity densities are again underpredicted for interacting nucleons by about a factor of 2. The corresponding calculation for Al is rather close to the data, underpredicting the experimental data for interacting nucleons by only about 30% and overpredicting the beam rapidity peak by about the same amount. As can be seen from Fig. 9, the calculations fall short in reproducing the beam rapidity peak for the Pb target. But there the discussion from the previous paragraph about a larger pedestal of interacting nucleons applies.

For the Al targets the baryon distributions have to be symmetric about $y=1.72$, and baryon number conservation gives 13.5 protons and 14 neutrons above midrapidity. Combining these numbers with our measurement of the number of noninteracting nucleons, one can obtain an estimate of the average inverse p_t slope constant of nucleons that have interacted. Using the results from Fig. 5 and the acceptance for beam rapidity nucleons we estimate that between rapidity 1.72 and 3.0 there have to be about 12 nucleons. If we make an assumption about the shape of the transverse momentum spectrum we can, from the intercepts displayed in Fig. 9, determine the slope constant of the transverse momentum spectrum. The proton data measured by experiment 802 at midrapidity [6] are well described by an exponential distribution of the invariant cross section as a function of the transverse mass m_t,

$$1/m_t\, d^2\sigma/dm_t dy = a\exp(-m_t/T)\ .$$

Inspecting the rapidity densities for Al in Fig. 9, a rather flat rapidity distribution for interacting protons is suggested. Based on a flat rapidity distribution we obtain for the total number of interacting protons

$$N=2a\int_{m_p}^{\infty} dm_t m_t \exp(-m_t/T)\int_{1.72}^{3.0} dy$$
$$=2.56a\ T(T+m_p)\exp(-m_p/T)\ .$$

At the same time the rapidity density at $p_t=0$ or $m_t=m_p$ is given as

$$I=a\exp(-m_p/T)\ .$$

We therefore can estimate the average slope constant from

$$T(T+m_p)=N/(2.56I)=24/(2.56\times 50)$$
$$=0.187\ \text{GeV}^2\ ,$$

leading to $T=0.17$ GeV. In this simple estimate this corresponds to the rapidity averaged inverse slope constant or temperature for protons from $y=0.44$–3.0. This estimate can be compared to results from experiment 802 in the backward hemisphere. There inverse slopes of 0.16 and 0.23 GeV have been obtained [20] at $y=0.55$ and 1.55 for their most central trigger. The corresponding rapidity distribution was found to be rather flat. These results bracket our estimated rapidity averaged value.

V. CONCLUSION

We have presented spectra of identified nucleons, measured in the E814 forward spectrometer with event characterization using transverse energy measurements in the backward hemisphere. The data clearly indicate the presence of a component of nucleons which emerge with beam rapidity and very low inverse p_t slope constant, even in central Si-nucleus collisions. From this component we have deduced the in-medium nucleon-nucleon cross section to be essentially unchanged from the "free" value of 29 mb, implying many collisions and small transparency.

Analysis of the measurement of the interacting component of the baryons near $p_t=0$ GeV/c reinforces this picture. The data agree in shape (but not in magnitude) with the predictions of the HIJET multiple collision code. At present this discrepancy is not understood and more complete measurements of identified particle spectra are necessary to shed more light on the situation. For nucleons that have interacted in Si+Al collisions we have deduced a mean inverse p_t slope constant of 0.17 GeV from an analysis of the spectra.

ACKNOWLEDGMENTS

We would like to thank the Brookhaven Tandem and AGS staff for excellent support and are in particular grateful for the expert help of W. McGahern, Dr. Y. Makdisi, and Dr. H. Brown. We would also like to thank R. Hutter and J. Sondericker without whom the experiment would not exist in its present form. Financial support by the U.S. DOE, the NSF, and the Canandian NSERC is gratefully acknowledged.

[1] M. Jacob, Nucl. Phys. **A498**, 1c (1989).
[2] R. J. Ledoux, Nucl. Phys. **A498**, 205c (1989); W. Busza and A. S. Goldhaber, Phys. Lett. **139B**, 235 (1984).
[3] J. Barrette *et al.*, E814 Collaboration, Phys. Rev. Lett. **64**, 1219 (1990).
[4] J. Barrette *et al.*, E814 Collaboration, submitted to Phys. Rev. C.
[5] J. Stachel, Nucl. Phys. **A525**, 23c (1991).
[6] T. Abbott *et al.*, E802 Collaboration, Phys. Rev. Lett. **64**, 847 (1990); Phys Rev. Lett. **66**, 1567 (1991).
[7] W. Love *et al.*, E810 Collaboration, Nucl. Phys. **A525**, 601c (1991).
[8] M. Fatyga, D. Makowiecki, and W. Llope, Nucl. Instrum. Methods **284**, 323 (1989).
[9] R. Brun, F. Bruyant, A. C. McPherson, and P. Zanarini, GEANT 3 Users Guide, CERN Data Handling Division Report No. DD/EE/84-1, 1984 (unpublished).
[10] R. Debbe *et al.*, IEEE Trans. Nucl. Sci. **37**, 88 (1990); J. Fischer *et al.*, *ibid.* **37**, 82 (1990).
[11] D. G. Cassel and H. Kowalski, Nucl. Instrum. Methods **185**, 235 (1981).
[12] H. Feshbach and K. Huang, Phys. Lett. **47B**, 300 (1973).
[13] A. S. Goldhaber, Phys. Lett. **53B**, 306 (1973).
[14] E. J. Moniz, I. Sick, R. R. Whitney, J. R. Ficenec, R. D. Kephart, and W. P. Trower, Phys. Rev. Lett. **26**, 445 (1971).
[15] S. Nagamiya, J. Randrup, and T. J. M. Symons, Annu. Rev. Nucl. Part. Sci. **34**, 155 (1984).
[16] *Total Cross Sections for Reactions of High Energy Particles*, edited by H. Schopper, Landoldt-Boernstein, New Series, Vol. 12 a, b (Springer-Verlag, Berlin, 1987).
[17] A. Shor and R. Longacre, Phys. Lett **218 B**, 100 (1989), based on Ref. [18].
[18] T. Ludlam, A. Pfoh, and A. Shor, in Proceedings of the RHIC Workshop I, Upton, NY, 1985, edited by P. Haustein and C. Woody [BNL Report No. 51921 (unpublished)].
[19] J. Stachel and P. Braun-Munzinger, Phys. Lett. **216 B**, 1 (1990); Nucl. Phys. **A495**, 393c (1989).
[20] M. A. Bloomer, Ph.D. thesis, MIT, 1990 (unpublished).